ARTICLES
PUBLISHED ONLINE: 6 APRIL 2015 | DOI: 10.1038/NNANO.2015.48
nature nanotechnology

A metal-free bifunctional electrocatalyst for oxygen reduction and oxygen evolution reactions

Jintao Zhang[1], Zhenghang Zhao[2], Zhenhai Xia[2] and Liming Dai[1]*

The oxygen reduction reaction (ORR) and oxygen evolution reaction (OER) are traditionally carried out with noble metals (such as Pt) and metal oxides (such as RuO_2 and MnO_2) as catalysts, respectively. However, these metal-based catalysts often suffer from multiple disadvantages, including high cost, low selectivity, poor stability and detrimental environmental effects. Here, we describe a mesoporous carbon foam co-doped with nitrogen and phosphorus that has a large surface area of ~1,663 $m^2 g^{-1}$ and good electrocatalytic properties for both ORR and OER. This material was fabricated using a scalable, one-step process involving the pyrolysis of a polyaniline aerogel synthesized in the presence of phytic acid. We then tested the suitability of this N,P-doped carbon foam as an air electrode for primary and rechargeable Zn–air batteries. Primary batteries demonstrated an open-circuit potential of 1.48 V, a specific capacity of 735 mAh g_{Zn}^{-1} (corresponding to an energy density of 835 Wh kg_{Zn}^{-1}), a peak power density of 55 mW cm^{-2}, and stable operation for 240 h after mechanical recharging. Two-electrode rechargeable batteries could be cycled stably for 180 cycles at 2 mA cm^{-2}. We also examine the activity of our carbon foam for both OER and ORR independently, in a three-electrode configuration, and discuss ways in which the Zn–air battery can be further improved. Finally, our density functional theory calculations reveal that the N,P co-doping and graphene edge effects are essential for the bifunctional electrocatalytic activity of our material.

Thanks to their high energy densities, rechargeable metal–air batteries have been targeted as a promising technology to meet the energy requirements for future electric vehicles and other energy-demanding devices[1–4]. The oxygen reduction reaction (ORR) and the oxygen evolution reaction (OER) are at the heart of metal–air batteries: oxygen molecules are reduced by electrons from the current collector and combine with metal dissolved in the electrolyte during discharging, and the reverse process occurs during charging. Among the metals targeted for this type of battery are Li and Zn, both of which are currently under intense scrutiny, but Zn–air batteries have the fundamental advantage of being less costly and safer[5–7]. One of the major challenges for Zn–air battery technology is to increase the O_2 reduction and evolution efficiencies, which will require the development of stable and effective bifunctional electrocatalysts, possibly working in aqueous electrolytes with air as the oxygen source[6,8]. Although precious metals such as Pt, Ru and Ir have been used as such electrocatalysts[9], their high cost and poor stability are hampering commercialization of the Zn–air battery technology.

Recent studies have shown that carbon nanomaterials (carbon nanotubes, graphene) doped with nitrogen could be an efficient, low-cost, metal-free alternative to Pt for ORR[10–13]. Co-doping N-doped carbon nanomaterials with a second heteroatom, such as B, S or P, can modulate the electronic properties and surface polarities to further increase ORR activity[14–17]. In contrast, most electrocatalysts reported for OER so far are based on transition-metal oxides[18] supported by carbon materials to facilitate electron transfer[19–24]. Although the development of metal-based bifunctional catalysts has recently attracted considerable attention[25,26], the use of carbon nanomaterials as bifunctional catalysts has rarely been discussed[27], and no truly metal-free bifunctional ORR and OER catalyst has been reported to date.

Here, we report a template-free method for the scalable fabrication of three-dimensional N and P co-doped mesoporous nanocarbon (NPMC) foams, simply by pyrolysis of polyaniline (PANi) aerogels synthesized in the presence of phytic acid (see Methods). The resultant NPMCs show bifunctional catalytic activities towards ORR and OER. As a result, Zn–air batteries fabricated with NPMCs show good performance and long-term stability.

Preparation and characterization of electrocatalyst

Aniline monomers were polymerized in the presence of phytic acid to produce a PANi hydrogel via a hard template-free gelation process[28] (Fig. 1a). To determine the optimum conditions for the formation of the PANi hydrogel, different ratios of aniline and phytic acid were examined (for more details see Supplementary Figs 1–4 and associated discussions in the Supplementary Information). After freeze-drying the resultant PANi hydrogel into aerogel (Fig. 1b), subsequent pyrolysis of the PANi aerogel led to the one-step formation of an NPMC foam (Fig. 1c and Supplementary Fig. 4). As can be seen in the insets of Fig. 1b,c, pyrolysis caused a slight shrinkage of the macroporous structure. The individual mesoporous ligaments (Fig. 1d) are highly interconnected into a hierarchical porous network. A transmission electron microscopy (TEM) image and associated elemental mapping (Fig. 1e) show the uniform distribution of C, N and P for a sample pyrolysed at 1,000 °C (NPMC-1000). Combined thermogravimetric analysis and mass spectrometry (TGA-MS), X-ray diffraction (XRD), Raman and TEM studies (Supplementary Figs 5–9) revealed that the pyrolysis converts most of the thermally stable domains (such as the benzene rings) into graphitic carbon domains that are co-doped with N and P from the PANi and phytic acid, respectively, accompanied by a release of decomposition gases (CO, CO_2 and so on, Supplementary Table 1). The resulting nanomaterial also possesses a large number of edge-like graphitic structures

[1]Center of Advanced Science and Engineering for Carbon (Case4carbon), Department of Macromolecular Science and Engineering, Case Western Reserve University, 10900 Euclid Avenue, Cleveland, Ohio 44106, USA. [2]Department of Materials Science and Engineering, Department of Chemistry, University of North Texas, Denton, Texas 76203, USA. *e-mail: liming.dai@case.edu

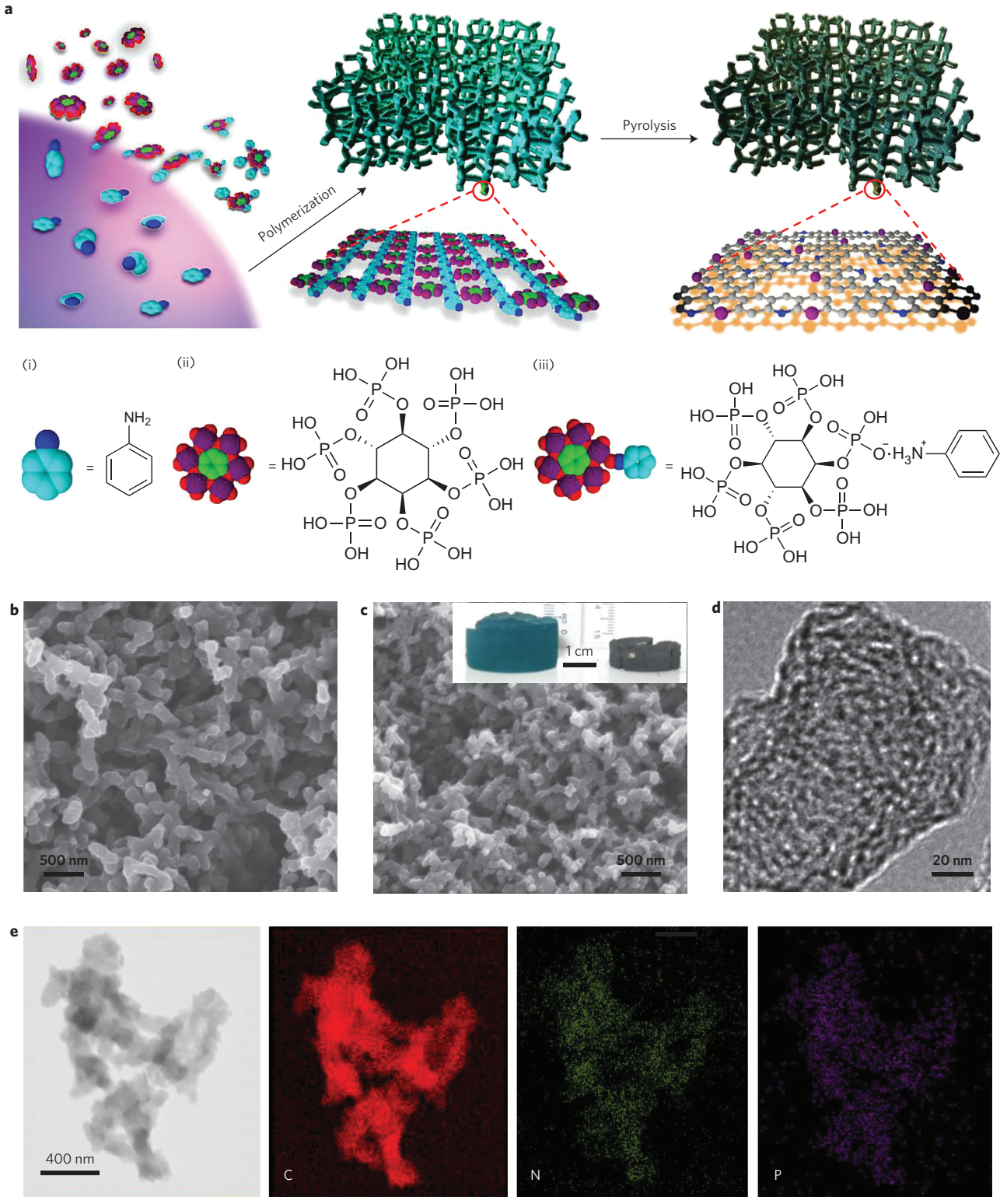

Figure 1 | Preparation of the N and P co-doped porous carbon (NPMC) electrocatalysts. a, Schematic illustration of the preparation process for the NPMC foams. An aniline (i)–phytic acid (ii) complex (iii) is formed (for clarity, only one of the complexed anilines is shown for an individual phytic acid), followed by oxidative polymerization into a three-dimensional PANi hydrogel crosslinked with phytic acids. As each phytic acid molecule can complex with up to six aniline monomers, phytic acid can be used as the crosslinker and protonic dopant to directly form the three-dimensional PANi hydrogel network; for clarity, only a piece of the two-dimensional network building block is shown in the enlarged view under the three-dimensional PANi hydrogel. The PANi hydrogel is freeze-dried into an aerogel and pyrolysed in Ar to produce the NPMC (for clarity, only a piece of the two-dimensional NPMC network building block is shown in the enlarged view under the three-dimensional NPMC). **b**,**c**, SEM images of PANi aerogel (**b**) and NPMC-1000 (**c**). Inset in **c**: Digital photo images of PANi aerogel before (left) and after (right) pyrolysis at 1,000 °C. **d**,**e**, High-resolution TEM image (**d**) and TEM image (**e**, left), with corresponding element mapping images of NPMC-1000 (**e**). The TEM image shows a piece of interconnected network-like scaffold. The element mapping images for C, N and P show a uniform distribution of the elements.

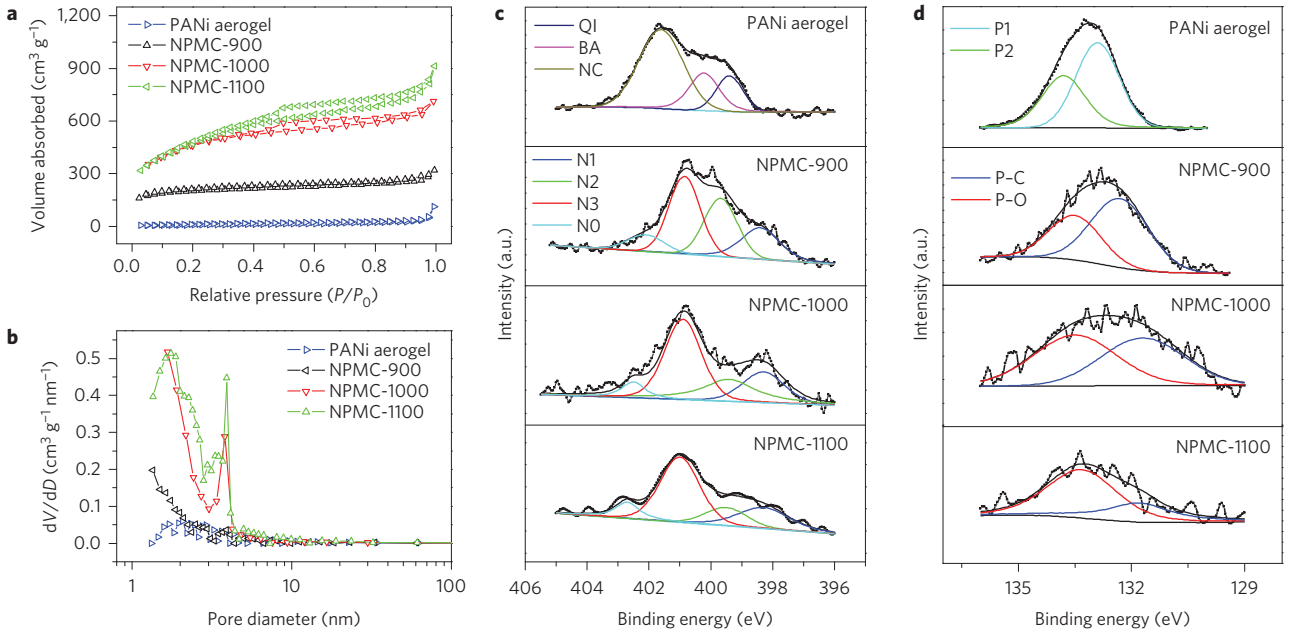

Figure 2 | Brunauer–Emmett–Teller characterization and XPS composition analysis. a,**b**, N_2 adsorption–desorption isotherms (**a**) and corresponding pore size distributions (**b**) for PANi aerogel, NPMC-900, NPMC-1000 and NPMC-1100. **c**,**d**, High-resolution XPS spectra of N_{1s} (**c**) and P_{2p} (**d**) for PANi aerogel, NPMC-900, NPMC-1000, and NPMC-1100. In **c**, for the PANi aerogel, the fitted peaks correspond to quinonoid imine (QI), benzenoid amine (BA) and nitrogen cationic radical (NC). In **c**, for NPMC samples, the fitted peaks correspond to oxidized pyridinic nitrogen (N0), pyridinic-N (N1), pyrrolic-N (N2) and graphitic-N (N3). In **d**, for the PANi aerogel, the fitted peaks correspond to P atoms in phosphate species (P1 and P2) with different binding energies. In **d**, for NPMC samples, the fitted peaks correspond to P-C and P-O.

(Supplementary Fig. 7), which play a crucial role in catalytic activity. Both the solution polymerization and the template-free pyrolysis process can be readily scaled up for low-cost mass production.

N_2 adsorption–desorption isotherm curves (Fig. 2a) for the NPMC samples exhibit absorbed volumes that are remarkably larger than that of the PANi aerogel and that increase significantly with increasing pyrolysis temperature. The specific surface areas (Supplementary Table 2) are also significantly enlarged on increasing the pyrolysis temperature of the PANi aerogel (53.5 $m^2\ g^{-1}$). In particular, there is a significant difference between the samples heated at 900 °C (NPMC-900, surface area of 635.6 $m^2\ g^{-1}$) and that heated at 1,000 °C (NPMC-1000, surface area of 1,548 $m^2\ g^{-1}$). The observed specific surface areas for NPMC-1000 and NPMC-1100 (1,663 $m^2\ g^{-1}$) are also much larger than those of hard template-synthesized porous carbons (~500–1,200 $m^2\ g^{-1}$)[11,15,29]. The more than doubled surface area of NPMC-1000 (compared with that of NPMC-900) agrees well with the significant weight loss around that temperature revealed by TGA-MS spectra (Supplementary Figs 5 and 6) due, most probably, to the generation of volatile species (CO, CO_2 and so on, also Supplementary Table 1) from carbonization of the PANi aerogel. The type IV isotherm curves shown in Fig. 2a have an obvious hysteresis and confirm the existence of mesopores. The rapid nitrogen uptake ($P/P_0 > 0.9$) might be due to the presence of secondary, much larger pores. Barrett–Joyner–Halenda (BJH) pore size distribution curves derived from the N_2 desorption branches confirm the presence of mesopores with diameters <10 nm (Fig. 2b) and significantly enhanced pore volumes from 0.17 $cm^3\ g^{-1}$ for the PANi aerogel to 0.50, 1.10 and 1.42 $cm^3\ g^{-1}$ for NPMC-900, NPMC-1000 and NPMC-1100 (Supplementary Table 2), respectively. Overall, our data confirm that the one-step pyrolysis process produces NPMC samples with three-dimensional mesoporous structures with large surface area, high pore volume and a pore size that is appropriate for electrocatalytic applications.

Typical X-ray photoelectron spectra (XPS) for NPMCs are provided in Supplementary Fig. 10, together with a summary of numerical data in Supplementary Table 2. As expected, the XPS spectra show peaks for C, N and P, as well as an O peak arising mainly from the phytic acid precursor (Fig. 1a). Nevertheless, the possibility of there being physically adsorbed oxygen in NPMCs cannot be ruled out, as the graphitic structure is known to be susceptible to oxygen absorption, even at low pressure[14]. The fitted XPS peaks for N_{1s} of the PANi aerogel (Fig. 2c) centred at ~399.5 eV, 400.3 eV and 401.6 eV are attributable to quinonoid imine, benzenoid amine and nitrogen cationic radicals, respectively. The presence of the NC peak is indicative of the protonic doping of PANi by phytic acid[30]. The XPS N_{1s} spectra for NPMC samples can be deconvoluted into four different bands at ~398.6, 400.5, 401.3 and 402.0 eV, which correspond to pyridinic (N1), pyrrolic (N2), graphitic (N3) and oxidized pyridinic (N0) nitrogen, respectively[31]. These various nitrogen species lead to different chemical/electronic environments for neighbouring carbon atoms and hence different electrocatalytic activities. The curve fitting in Fig. 2c and the corresponding normalized results (Supplementary Fig. 11) indicate a conversion from pyrrolic to graphitic nitrogen with increasing temperature, consistent with previous reports on N-doped carbon materials[32]. The P_{2p} spectra (Fig. 2d) of the PANi aerogel were deconvoluted into two different bands at ~132.9 eV (P1) and 133.8 eV (P2), corresponding to the core levels of P atoms in phosphate species[33]. Following heat treatment, NPMC-900 showed two similar component peaks with a slight binding shift to lower energy, arising from gradual dehydration and condensation of phosphoric groups into polyphosphates, and the subsequent charge-transfer interaction of P with conjugated aromatic C rings to generate P–C (131.8 eV) and P–O (133.4 eV) bonds in NPMC-1000 and NPMC-1100[34,35]. This suggests the successful doping of P heteroatoms into the carbon network through thermal pyrolysis[35]. Further heating caused a gradual loss of the P–C peak due to thermal decomposition of heteroatom dopants from the carbon matrix (Supplementary Table 2), consistent with our TGA and TGA-MS results (Supplementary Figs 5 and 6). Thus, it is critical

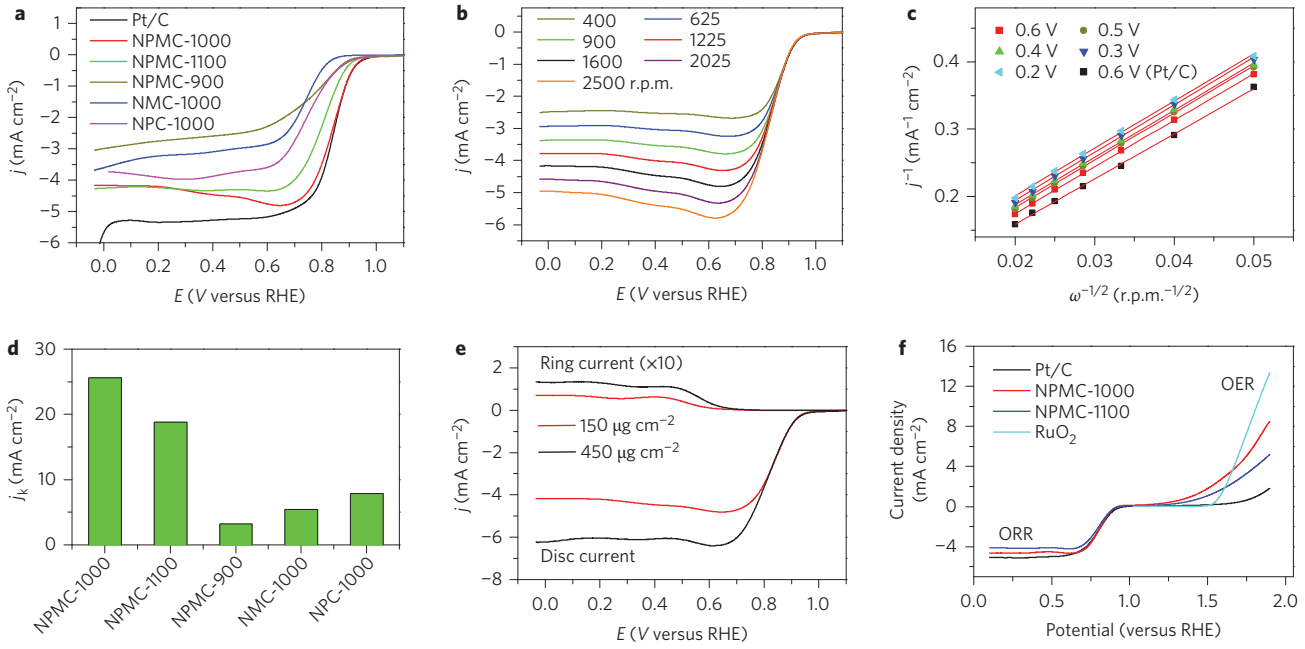

Figure 3 | Electrocatalytic activity for ORR and OER. a, Linear scan voltammogram (LSV) curves for NPMC-900, NPMC-1000, NPMC-1100, NMC-1000, NPC-1000 and commercial Pt/C catalyst at an RDE (1,600 r.p.m.) in O_2-saturated 0.1 M KOH solution. Scan rate, 5 mV s^{-1}. **b**, LSV curves of NPMC-1000 in oxygen-saturated 0.1 M KOH at various rotating speeds. **c**, K-L plots for NPMC-1000 and Pt/C at various potentials. **d**, Kinetic current of various samples for O_2 reduction at 0.65 V. **e**, RRDE measurements (1,600 r.p.m.) of ORR at an NPMC-1000 electrode with different catalyst loadings. **f**, LSV curves of NPMC-1000, NPMC-1100, RuO_2 and commercial Pt/C catalyst on an RDE (1,600 r.p.m.) in 0.1 M KOH (scan rate, 5 mV s^{-1}), showing the electrocatalytic activities towards both ORR and OER.

to control the pyrolysis temperature to produce NPMCs with the desired mesopores as well as N and P contents.

Electrochemical evaluation of NPMCs for ORR and OER

Cyclic voltammetry (CV) curves (Supplementary Fig. 12) were found to exhibit oxygen reduction peaks for all the NPMC electrodes in O_2-saturated KOH solution, but not the N_2-saturated KOH solution. The observed oxygen reduction peak shifted to more positive potentials with increasing pyrolysis temperature from 800 to 1,000 °C, but slightly reversed on further increasing the temperature to 1,100 °C. A reduction potential similar to that of the commercial Pt/C catalyst Pt/XC-72 (20 wt%) was observed at the NPMC-1000 electrode, suggesting a high electrocatalytic activity of the metal-free NPMC catalyst. This is because pyrolysis at a higher temperature normally leads to a higher degree of graphitization, with higher electrical conductivity (thus a lower charge-transfer resistance in Supplementary Fig. 13) and hence better electrocatalytic activity (as from NPMC-900 to NPMC-1000). However, overheating (say from 1,000 to 1,100 °C) could lead to decomposition of the dopants (Supplementary Table 2) and hence the observed negative shift of the peak potential from NPMC-1000 to NPMC-1100. The current density follows the same trend (Supplementary Fig. 12), indicating once again that NPMC-1000 is more electrocatalytically active than both NPMC-900 and NPMC-1100.

The linear scan voltammogram (LSV) curves in Fig. 3a confirm the electrocatalytic performance of NPMC-1000, with a positive onset potential of 0.94 V versus reversible hydrogen electrode (RHE) and a half-wave potential of 0.85 V versus RHE. These values are comparable to those of Pt/C, and outperform most previously reported metal-free ORR catalysts[29,36] and even recently reported carbon-based catalysts with metals[27,37,38]. Furthermore, the limiting current of the NPMC-1000 electrode is much larger than those of the NPMC-900 and NPMC-1100 electrodes, and is comparable to that of Pt/C (Fig. 3a). Also included in Fig. 3a are the corresponding LSV curves for the purely N-doped mesoporous carbon (NMC-1000; see Methods) and N- and P-doped carbon (NPC-1000; see Methods). As can be seen, the NPMC-1000 has the highest electrocatalytic activity of all the aforementioned metal-free catalysts in terms of both the onset potential and limiting current, highlighting the importance of the N,P co-doping and mesoporous structure for ORR. The electron transfer number per oxygen molecule (n) for ORR was determined from the LSV curves (Fig. 3b,c and Supplementary Fig. 14) according to the Koutechy–Levich (K–L) equation (for details see Supplementary Information). The K–L plots (Fig. 3c) show linear relationships between j_k^{-1} and $\omega^{-1/2}$ (where j_k is the kinetic current and ω is the electrode rotating rate), with a similar slope for the NPMC-1000 and Pt/C electrodes, from which n was determined to be ~4.0, suggesting a four-electron pathway for ORR[11,13]. The kinetic current obtained from the intercept of the linearly fitted K–L plots at 0.65 V (versus RHE) for the NPMC-1000 electrode is the largest among all the metal-free catalysts investigated in this study (Fig. 3d). Although the NPMC-900 sample has the highest N and P contents (Supplementary Table 2), the relatively low pyrolysis temperature could lead to a high charge-transfer resistance (Supplementary Fig. 13) and hence a relatively poor electrocatalytic activity. Although the electrical conductivity could be enhanced by increasing the pyrolysis temperature, the doped heteroatoms would be removed (Supplementary Table 2), resulting in a reduction in the active sites and overall electrocatalytic activity, as exemplified by NPMC-1100 (Fig. 3a).

To further evaluate the ORR pathways for the NPMC-1000 electrode, we performed rotating ring–disk electrode (RRDE) measurements. As shown in Fig. 3e, NPMC-1000 electrodes with two different mass loadings (150 and 450 μg cm^{-2}) exhibited high disk current densities (~4 and 6 mA cm^{-2}) for O_2 reduction and much lower ring current densities (~0.007 and 0.014 mA cm^{-2}) for peroxide oxidation. Notably, the disk current could be enhanced significantly by increasing the mass loading and even become larger

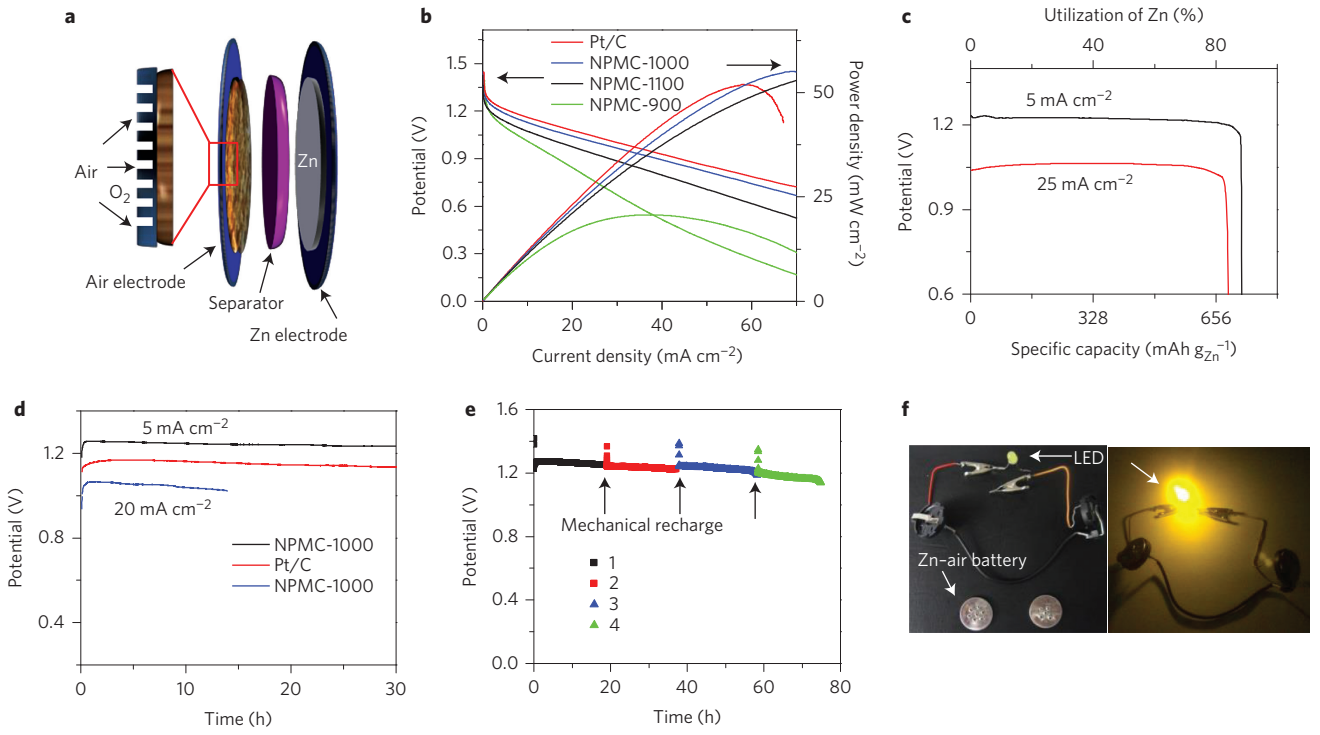

Figure 4 | Performance of a primary Zn–air battery. a, Schematic of the basic configuration of a primary Zn–air battery, in which a carbon paper pre-coated with NPMC is used as an air cathode and is coupled with a Zn anode and a glassy fibre membrane soaked with aqueous KOH electrolyte as the separator. The enlarged part illustrates the porous air electrode loaded with electrocatalyst, which is permeable to air. **b**, Polarization and power density curves of primary Zn–air batteries using Pt/C, NPMC-900, NPMC-1000, NPMC-1100 as ORR catalyst (mass loading of 0.5 mg cm^{-2}) and 6 M KOH electrolyte (scan rate, 5 mV s^{-1}). **c**, Specific capacities of the Zn–air batteries using NPMC-1000 as ORR catalyst are normalized to the mass of the consumed Zn. **d**, Discharge curves of the primary Zn–air batteries using Pt/C and NPMC-1000 as ORR catalyst and KOH electrolyte at various current densities (5 and 20 mA cm^{-2}). The observed sudden drop in voltage at 0 h was caused by a sudden increase in current density after resting the battery at the open-circuit potential without current loading for the testing. **e**, Long-time durability of the primary Zn–air battery using NPMC-1000 catalyst at a current density of 2 mA cm^{-2}. The battery is mechanically rechargable. The Zn and electrolyte were mechanically replaced at the point where the colour of the curve changes (the numbers represent the first, second, third and fourth charge cycles). Coloured symbols above the curve are taken from the open-circuit potential by opening the battery for each mechanical recharge. **f**, Optical images of an LED (~2.2 V) before and after being driven by two Zn–air batteries in series.

than that of Pt/C. Supplementary Fig. 15a shows the percentage of peroxide species with respect to the total oxygen reduction products, and Supplementary Fig. 15b shows the electron transfer numbers calculated from the RRDE curves (for details see Supplementary Information). It can be envisioned that oxygen molecules were reduced to water via a nearly four-electron pathway (n is over 3.85) with a small ratio of peroxide species (less than 8%). Similar good electrocatalytic activities were also observed for NPMC-1000 in 1 and 6 M KOH electrolytes (Supplementary Figs 16 and 17). In comparison with the Pt/C catalyst, the NPMC-1000 electrode exhibited better long-term stability, higher resistance to the methanol cross-over effect and CO poisoning effect (Supplementary Fig. 18) in oxygen-saturated 0.1 M KOH, and comparable catalytic activity, even in acidic electrolyte (Supplementary Figs 19 and 20). Because the activation energy of ORR on a catalyst is directly related to its catalytic activity[17,39], we used first-principles methods to calculate the activation energy of ORR elemental steps in acidic and alkaline environments. As depicted in Supplementary Table 3, of the five barriers in acidic media, H_2O formation in the last step of the ORR has the highest value (0.66 eV) and is therefore the rate-limiting step for ORR (and is much smaller than that of a Pt(111) surface (1.22 eV)[40]). In alkaline media, our calculated activation energy for the rate-limiting step of the Langmuir–Hinshelwood mechanism is ~0.5 eV for N,P co-doped graphene, while the activation energies for N-doped graphene and on a Pt(111) surface are ~0.56–0.62 eV and 0.55 eV, respectively[40,41]. Our calculations (shown in Fig. 6, in the following) also reveal that NPMCs possess ORR activities comparable to, or even better than, that of Pt in alkaline media. Thus, the N,P co-doped carbon could show high catalytic activities in both acidic and alkaline environments.

Figure 3f shows the rapidly increased anodic current above ~1.30 V associated with OER. The good OER catalytic activities for NPMCs were reflected by their lower onset potentials and higher currents than those of the Pt/C electrode (Fig. 3f). As a reference, we also used a state-of-the-art OER electrode based on RuO_2 nanoparticles (see Supplementary Information for synthesis and Supplementary Fig. 21)[42], and found that the NPMC-1000 electrode exhibited a lower onset potential than the RuO_2 nanoparticles, though slightly lower current densities at higher potentials (Fig. 3f, see also Supplementary Fig. 22 in 6 M KOH).

NPMC as an air cathode in primary Zn–air battery

Bifunctional catalysts for both ORR and OER are highly desirable for use in rechargeable Zn–air battery applications. To this end we explored the possibility of using NPMC as a metal-free bifunctional catalyst. We first constructed a primary Zn–air battery using NPMC as the electrocatalyst (Fig. 4a). The open-circuit potential (OCP) of this two-electrode primary Zn–air battery is as high as ~1.48 V (Supplementary Fig. 23), suggesting a good catalytic performance of NPMC-1000, even in this cell configuration. Figure 4b presents polarization and power density curves for

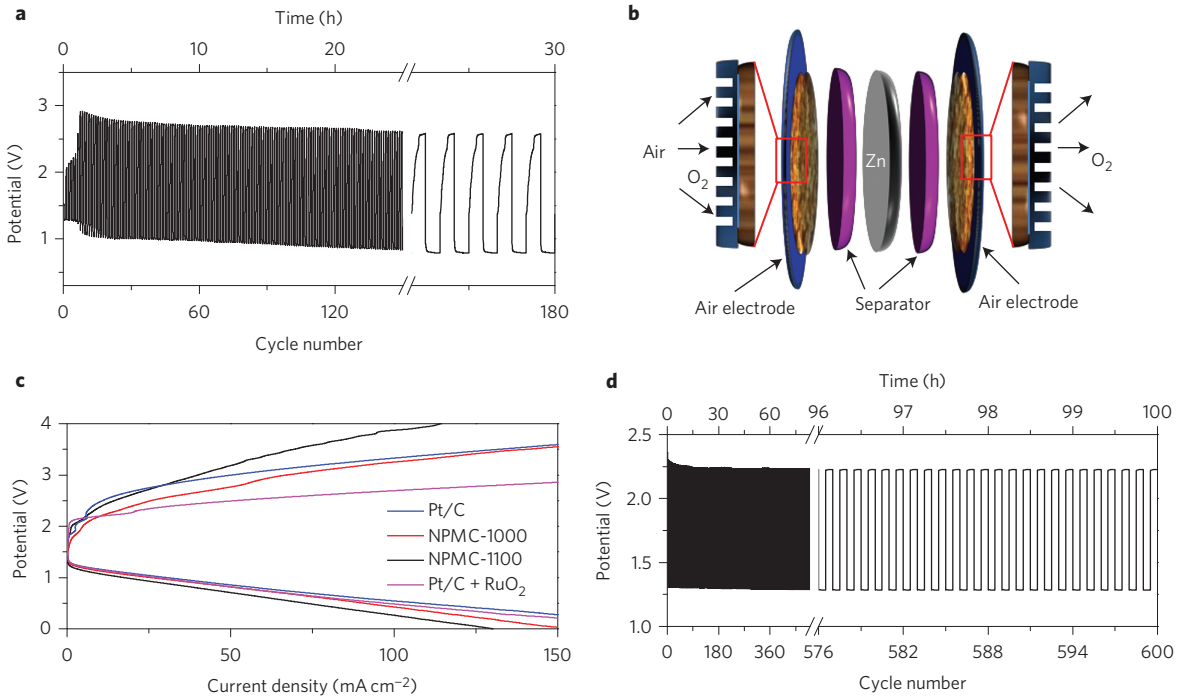

Figure 5 | Performance of rechargeable Zn–air batteries. a, Discharge/charge cycling curves of two-electrode rechargeable Zn–air batteries at a current density of 2 mA cm^{-2} using the NPMC-1000 air electrode. **b**, Schematic of the basic configuration of a three-electrode Zn–air battery by coupling the Zn electrode with two air electrodes to separate ORR and OER. The enlarged parts illustrate the porous structures of the air electrodes, which facilitates gas exchange. **c**, Charge and discharge polarization curves of three-electrode Zn–air batteries using NPMC-1000, NPMC-1100 or commercial Pt/C catalyst as both air electrodes, together with the corresponding curve (that is, Pt/C + RuO_2) for the three-electrode Zn–air battery with Pt/C and RuO_2 nanoparticles as each of the air electrodes, respectively. **d**, Discharge/charge cycling curves of a three-electrode Zn–air battery using NPMC-1000 for the air electrodes (0.5 mg cm^{-2} for ORR and 1.5 mg cm^{-2} for OER) at a current density of 2 mA cm^{-2}.

Zn–air batteries based on the NPMC air cathodes. The NPMC-1000 catalyst showed a current density of ~70 mA cm^{-2} and a peak power density of ~55 mW cm^{-2}, comparable to those of a Pt/C catalyst (~60 mA cm^{-2} and 50 mW cm^{-2}). The good performances of our NPMC-1000 foam derive from its porous structure, which facilitates an efficient diffusion of O_2 gas and electrolyte to the active sites. When normalized to the mass of consumed Zn, the specific capacity of our battery was over 735 mAh g_{Zn}^{-1} (corresponding to an energy density of ~835 Wh kg_{Zn}^{-1}) at a current density of 5 mA cm^{-2}, which corresponds to ~89.6% utilization of the theoretical capacity (~820 mAh g_{Zn}^{-1})[5] (Fig. 4c). When the current density was increased to 25 mA cm^{-2}, the specific capacity of the battery was ~689 mAh g_{Zn}^{-1} (corresponding to an energy density of ~695 Wh kg_{Zn}^{-1}). These values are higher than those of Zn–O_2 batteries that use a metal-oxide-based CoO/CNT catalyst (~570 Wh kg_{Zn}^{-1} at 10 mA cm^{-2})[6]. Notably, the potential of the battery using NPMC-1000 (~1.26 V) at the current density of 5 mA cm^{-2} is also higher than batteries using Pt/C (~1.16 V). Furthermore, no significant potential drop was observed under galvanostatic discharge for 30 h at 5 mA cm^{-2} and 14 h at 20 mA cm^{-2} (Fig. 4d), indicating a good catalytic stability for ORR. Although Zn is gradually consumed during the discharging process, the battery can be mechanically recovered by refilling the Zn plate and KOH electrolyte. Typically, our battery can continue to work over 240 h with almost no potential decrease during two cycles (Supplementary Fig. 24), comparing favourably with most other recently reported primary Zn–air batteries (Supplementary Table 4). The battery can be mechanically charged for many cycles (Fig. 4e). Our Zn–air battery can also be operated in KOH electrolyte at a lower concentration (1.0 M KOH) with excellent durability (Supplementary Fig. 25). To meet specific energy and/or power needs for various practical applications, multiple Zn–air batteries can be integrated into series circuits. As exemplified in Supplementary Fig. 23, two Zn–air button batteries were connected in series to generate a sufficiently high OCP of ~2.8 V to power different light-emitting diodes (LEDs) (Fig. 4f and Supplementary Fig. 26).

NPMC as an air cathode in rechargeable Zn–air battery

We also developed a rechargeable Zn–air battery[1,4]. In a rechargeable Zn–air battery, the kinetics is mainly limited by the cathode reaction[5]:

$$O_2 + 2H_2O + 4e^- \underset{\text{OER}}{\overset{\text{ORR}}{\rightleftharpoons}} 4OH^-$$

A two-electrode rechargeable Zn–air battery with NPMC-1000 as its bifunctional catalyst (Supplementary Fig. 27) showed good rechargeability, as evidenced by 180 discharge/charge cycles over a period of 30 h (Fig. 5a), which is better than the performance of a Zn–air battery using core-corona-structured bifunctional catalyst with lanthanum nickelate centres supporting N-doped carbon nanotubes (75 cycles for 12.5 h)[8] and a MnO_2/Co_3O_4 hybrid (60 cycles for 14 h) catalyst[43]. With the relatively poor catalytic activity of Pt/C for OER in mind, for comparison we also fabricated a reference two-electrode Zn–air battery using mixed Pt/C and RuO_2 as a bifunctional electrocatalyst for ORR and OER (Supplementary Fig. 28). Compared with Fig. 5a, the results in Supplementary Fig. 28 show a lower charging potential, indicating a relatively high catalytic activity towards OER.

Although NPMC-1000 accelerates both ORR and OER, a certain degree of irreversibility is unavoidable due to the different catalytic activities of the same catalyst toward the ORR and OER reactions. Consequently, a deteriorating performance was observed for the two-electrode rechargeable Zn–air battery during a long-term cycling test (Supplementary Fig. 29)[8]. However, the catalytic

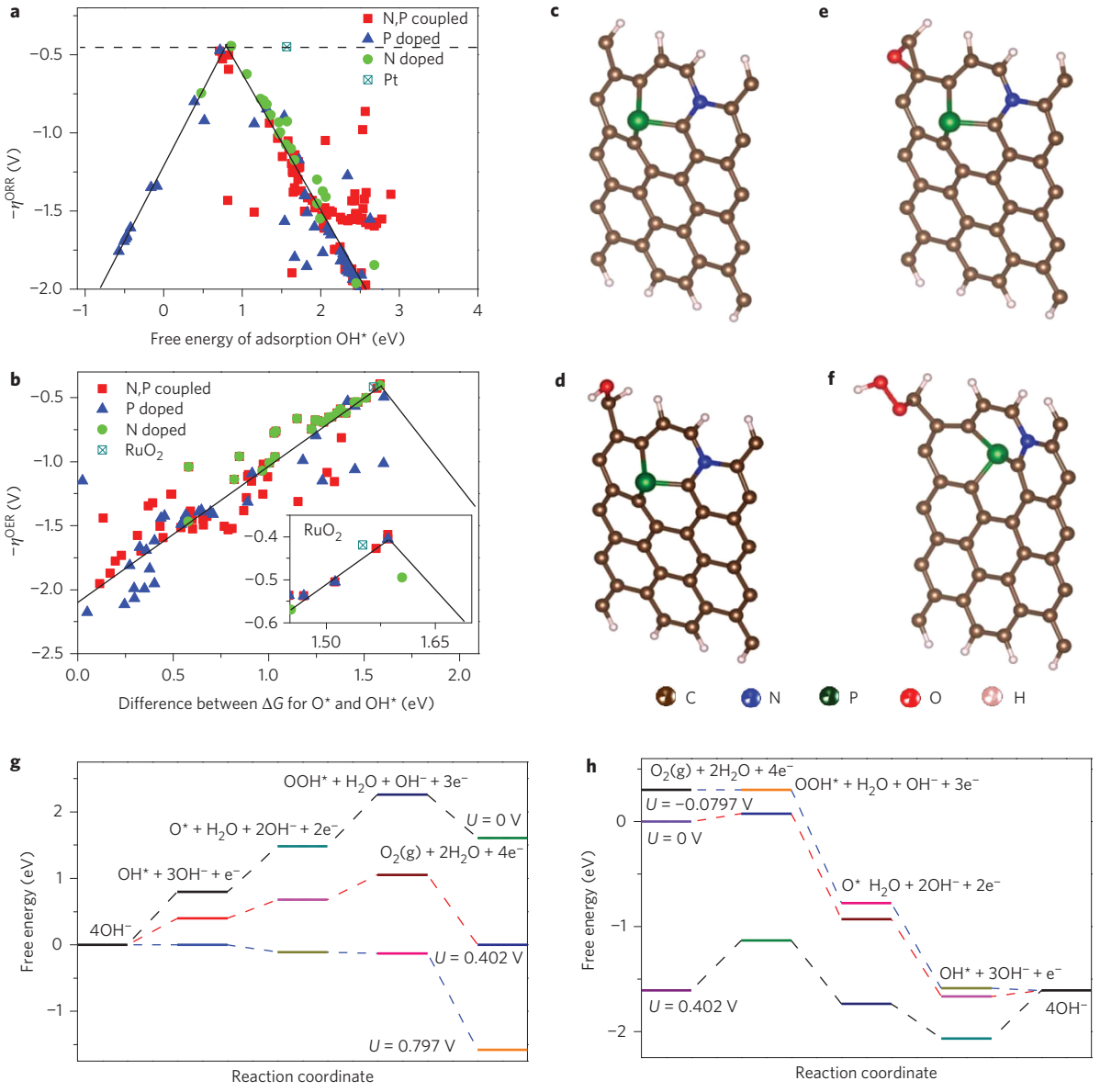

Figure 6 | Mechanistic study of bifunctionality for ORR and OER. a,**b**, ORR (**a**) and OER (**b**) volcano plots of overpotential η versus adsorption energy of O* and the difference between the adsorption energy of O* and OH*, respectively, for N-doped, P-doped and N,P-doped graphene. **c**–**f**, Initial structure (**c**) and structures after the adsorption of hydroxyl OH* (**d**), oxyl O* (**e**) and peroxyl OOH* (**f**) intermediates on N and P coupled graphene. O*, OH* and OOH* are adsorbed intermediates. The overpotentials of the best catalysts predicted theoretically for ORR (Pt) (ref. 47) and OER (RuO_2) (ref. 42) are also plotted in **a** and **b**, respectively. Inset in **b**: Detail of the volcano top in the main panel. **g**,**h**, Schematic energy profiles for the OER pathway (**g**) and the ORR pathway (**h**) on N,P co-doped graphene in alkaline media.

activity of NPMC can be improved by optimizing the pore structure, the heteroatom doping site, electrode surface chemistry and cell configuration. Indeed, the NPMC battery performance was significantly enhanced by using an optimized three-electrode configuration (Fig. 5b), which prevents the bifunctional catalyst from coming into contact with the oxidative (or reductive) potential during ORR (or OER). In this case, the activities toward ORR and OER could be independently regulated by adjusting the catalyst mass loading on each of the two air electrodes[6,44], and a balanced reversible transfer between oxygen reduction and evolution was readily achieved. Figure 5c shows the discharge and charge polarization curves for the three-electrode batteries with various air electrodes. The three-electrode rechargeable Zn–air battery using NPMC-1000 for the air electrodes showed no obvious voltage change over 600 discharge/charge cycles (for 100 h, Fig. 5d), which is comparable to that of a three-electrode Zn–air battery using Pt/C and RuO_2 as the ORR and OER catalysts, respectively (Supplementary Fig. 30). As shown in Supplementary Table 5, our battery is comparable to, or even better than, most of the recently reported rechargeable Zn–air batteries based on metal/metal-oxide electrodes[6,45,46].

Mechanistic study on ORR and OER of bifunctional NPMCs

To gain further insights into the ORR and OER catalytic mechanisms of NPMC, we performed first-principles calculations using density functional theory (DFT) methods to determine the electronic structures and catalytic reactions for the N,P co-doped carbon structures (Fig. 6). In the co-doped structure, N and P may exist on the graphene in different forms, such as the isolated N-dopant, the isolated P-dopant and/or as N,P-coupled dopants (in which N and P are close to each other). To study the ORR/OER catalytic activities of these structures, all possible types

of doping structure were built, as shown in Supplementary Fig. 31. Furthermore, the doping positions in each of the structures were changed with respect to the graphene edge to reveal the effect of doping sites. The possible ORR and OER pathways on N,P co-doped graphene are listed in Supplementary equations (1) to (13) (Supplementary Section 4). As the overpotential η of ORR/OER is an important measure of the catalytic activities of a catalyst[47], we calculated the overpotential for each active site on the doped structures and determined the minimum overpotential for ORR and OER. An ideal catalyst should be able to facilitate ORR and OER just above the equilibrium potential, with zero overpotential. However, the ideal case cannot be achieved because the binding energies of the intermediates are correlated[47]. Thus, thermodynamically, the lower overpotential indicates the better catalyst. Figure 6a,b presents volcano plots, that is, the overpotential versus descriptors for various reaction sites on N,P co-doped graphene structures in alkaline environments. From this theoretical analysis, the isolated N-doped, the isolated P-doped and the N,P-coupled structures were identified to have minimum ORR overpotentials of 0.44, 0.47 and 0.47 V, respectively, while the lowest OER overpotentials for these structures were 0.41, 0.49 and 0.39 V, respectively. Note that the N,P-coupled doping gives the best OER performance, while the ORR overpotential could reach as low as 0.44 V based on the estimate of the volcano plot (Fig. 6a). Overall, the minimum overpotentials of N,P co-doped graphene for ORR and OER are 0.44 V and 0.39 V respectively, lower than those of the best catalysts identified theoretically (~0.45 V for ORR on Pt[47] and ~0.42 V for OER on RuO_2[42]), indicating that the bifunctional N,P co-doped graphene catalyst could outperform its metal/metal-oxide counterparts. Clearly, the N and P co-doping generates synergistic effects to improve the electrocatalytic activities towards both OER and ORR.

For OER, the most active structure was identified to be the N,P-coupled graphene shown in Fig. 6c, with the active site located at the edge of the graphene. The elementary reactions of OER over graphene in an alkaline environment are shown in Fig. 6d–f. For the active sites on this graphene, the OER is uphill when the electrode potential is 0 V, but when the potential increases to 0.797 V (0.395 V in overpotential), all the elementary reaction steps become downhill and OER occurs spontaneously over 0.797 V (Fig. 6g). Because the OER overpotential is reduced by the co-doping, the OER is facilitated overall by the N,P co-doped graphene. Similar phenomena are observed for ORR, but the reaction active sites are different from those for OER, although they are also located near the graphene edges[48]. The most active site was identified to be N-dopant (elementary reaction pathways have been described for N-doped graphene in our previous papers[39,49]). For ORR, the most active site is also located at the edge and the elementary reactions and energy change are shown in Fig. 6h. OOH formation is the rate-determining step of ORR, and is endothermic in alkaline media under a voltage of 0.402 V. At zero external potential all reactions are downhill, except for O_2 adsorption, which has a small energy barrier that disappeared at −0.0797 V. Overall, the distance of the doping sites from the graphene edge seems critical to the adsorption of chemical species and catalytic activity. In most cases, OER and ORR usually occur near the edge of the graphene, but at different sites.

Conclusions

We have developed a low-cost and scalable approach to prepare three-dimensional mesoporous carbon foams co-doped with N and P (NPMCs), simply by pyrolysing polyaniline aerogels obtained from a template-free polymerization of aniline in the presence of phytic acid. The resultant NPMCs show efficient catalytic activities for both ORR and OER as bifunctional air electrodes in primary and rechargeable Zn–air batteries. Typically, our primary battery based on the NPMC metal-free air electrode operating in ambient air with an aqueous KOH electrolyte exhibited an open-circuit potential of ~1.48 V, an energy density of ~835 Wh kg_{Zn}^{-1} and a peak power density of ~55 mW cm^{-2}, as well as excellent durability (over 240 h of operation after two mechanical recharges). A three-electrode rechargeable battery using two NPMC metal-free air electrodes to separate ORR and OER also showed good stability (600 cycles for 100 h of operation). First-principles simulations revealed that the N and P co-doping and the highly porous network of the carbon foam are crucial to generating bifunctional activity towards both ORR and OER. We anticipate that our nanomaterial will also be useful for other electrocatalytic applications.

Methods

Preparation of NPMCs. PANi aerogel was prepared by oxidative polymerization in the presence of phytic acid according to a published procedure[28]. Typically, 5 ml of aniline monomer was added into 20 ml phytic acid solution (16%, wt/wt in water). Ammonium persulphate (APS, 0.96 g) was dissolved in 10 ml deionized water under stirring. After cooling to 4 °C, the two solutions were mixed together and kept overnight without stirring. The resultant hydrogel was washed by immersion in deionized water for two days then freeze-dried for 24 h to produce polyaniline aerogel for pyrolysis. To prepare N,P co-doped mesoporous carbon (NPMC) foams, the PANi aerogel was calcined at the desired temperatures (900, 1,000 and 1,100 °C) for 2 h under argon. The obtained samples were designated NPMC-900, NPMC-1000 and NPMC-1100, respectively. For comparison, phytic acid was removed from the PANi hydrogel by a de-doping process against $NH_3{\cdot}H_2O$ washing. The pure N-doped mesoporous carbon foam was then prepared by annealing the de-doped PANi aerogel at 1,000 °C (designated NMC-1000). N and P co-doped carbon (NPC-1000) and RuO_2 nanoparticles were also synthesized as references (for preparation processes see Supplementary Information).

Electrocatalytic activity evaluation. All electrochemical measurements were conducted in a three-electrode configuration at room temperature (~25 °C). The potential, measured against an Ag/AgCl electrode, was converted to potential versus RHE according to $E_{vs\ RHE} = E_{vs\ Ag/AgCl} + E_{ø\ Ag/AgCl} + 0.059$ pH. To prepare the working electrode, 5 mg of NPMC samples were dispersed in an aqueous solution containing 0.95 ml deionized water and 0.05 ml of 5 wt% Nafion under sonication. The obtained homogeneous catalyst ink (6 µl) was dropped onto a mirror-polished glassy carbon electrode. The mass loading was 0.15 mg cm^{-2} unless otherwise noted. The Pt/C (20 wt%, ETEK) electrode was prepared using the same procedure. A 0.1 M KOH aqueous solution saturated with oxygen was used as the electrolyte unless otherwise stated.

For the Zn–air battery test, the air electrode was prepared by uniformly coating the as-prepared catalyst ink onto carbon paper (SPECTRACARB 2040-A, Fuel Cell store) then drying it at 80 °C for 2 h. The mass loading was 0.5 mg cm^{-2} unless otherwise noted. A Zn plate was used as the anode. Both electrodes were assembled into a home-made Zn–air battery, and 6 M KOH aqueous solution was used as the electrolyte unless otherwise stated. The same procedure was used to prepare air electrodes with a catalyst mass ratio of 1:3 as the ORR and OER electrodes, in a three-electrode rechargeable Zn–air battery.

Received 30 April 2014; accepted 16 February 2015; published online 6 April 2015

References

1. Dunn, B., Kamath, H. & Tarascon, J-M. Electrical energy storage for the grid: a battery of choices. *Science* **334,** 928–935 (2011).
2. Peng, Z., Freunberger, S. A., Chen, Y. & Bruce, P. G. A reversible and higher-rate Li–O_2 battery. *Science* **337,** 563–566 (2012).
3. Park, M., Sun, H., Lee, H., Lee, J. & Cho, J. Lithium-air batteries: survey on the current status and perspectives towards automotive applications from a battery industry standpoint. *Adv. Energy Mater.* **2,** 780–800 (2012).
4. Goodenough, J. B. Evolution of strategies for modern rechargeable batteries. *Acc. Chem. Res.* **46,** 1053–1061 (2013).
5. Kraytsberg, A. & Ein-Eli, Y. The impact of nano-scaled materials on advanced metal–air battery systems. *Nano Energy* **2,** 468–480 (2013).
6. Li, Y. *et al.* Advanced zinc–air batteries based on high-performance hybrid electrocatalysts. *Nature Commun.* **4,** 1805 (2013).
7. Lee, J-S. *et al.* Metal–air batteries with high energy density: Li–air versus Zn–air. *Adv. Energy Mater.* **1,** 34–50 (2011).
8. Chen, Z. *et al.* Highly active and durable core–corona structured bifunctional catalyst for rechargeable metal–air battery application. *Nano Lett.* **12,** 1946–1952 (2012).
9. Morales, L. & Fernandez, A. M. Unsupported $Pt_xRu_yIr_z$ and Pt_xIr_y as bi-functional catalyst for oxygen reduction and oxygen evolution reactions in acid media, for unitized regenerative fuel cell. *Int. J. Electrochem. Sci.* **8,** 12692–12706 (2013).

10. Gong, K., Du, F., Xia, Z., Durstock, M. & Dai, L. Nitrogen-doped carbon nanotube arrays with high electrocatalytic activity for oxygen reduction. *Science* **323,** 760–764 (2009).
11. Liu, R., Wu, D., Feng, X. & Müllen, K. Nitrogen-doped ordered mesoporous graphitic arrays with high electrocatalytic activity for oxygen reduction. *Angew. Chem. Int. Ed.* **49,** 2565–2569 (2010).
12. Wang, S. *et al.* BCN graphene as efficient metal-free electrocatalyst for the oxygen reduction reaction. *Angew. Chem. Int. Ed.* **51,** 4209–4212 (2012).
13. Zheng, Y., Jiao, Y., Ge, L., Jaroniec, M. & Qiao, S. Z. Two-step boron and nitrogen doping in graphene for enhanced synergistic catalysis. *Angew. Chem. Int. Ed.* **52,** 3110–3116 (2013).
14. Wang, S. *et al.* Vertically aligned BCN nanotubes as efficient metal-free electrocatalysts for the oxygen reduction reaction: a synergetic effect by co-doping with boron and nitrogen. *Angew. Chem. Int. Ed.* **50,** 11756–11760 (2011).
15. Liang, J., Jiao, Y., Jaroniec, M. & Qiao, S. Z. Sulfur and nitrogen dual-doped mesoporous graphene electrocatalyst for oxygen reduction with synergistically enhanced performance. *Angew. Chem. Int. Ed.* **51,** 11496–11500 (2012).
16. Xue, Y. *et al.* Three-dimensional B,N-doped graphene foam as a metal-free catalyst for oxygen reduction reaction. *Phys. Chem. Chem. Phys.* **15,** 12220–12226 (2013).
17. Jiao, Y., Zheng, Y., Jaroniec, M. & Qiao, S. Z. Origin of the electrocatalytic oxygen reduction activity of graphene-based catalysts: a roadmap to achieve the best performance. *J. Am. Chem. Soc.* **136,** 4394–4403 (2014).
18. Grimaud, A. *et al.* Double perovskites as a family of highly active catalysts for oxygen evolution in alkaline solution. *Nature Commun.* **4,** 2439 (2013).
19. Chen, S., Duan, J., Jaroniec, M. & Qiao, S. Z. Three-dimensional N-doped graphene hydrogel/NiCo double hydroxide electrocatalysts for highly efficient oxygen evolution. *Angew. Chem. Int. Ed.* **52,** 13567–13570 (2013).
20. Zhao, Y., Nakamura, R., Kamiya, K., Nakanishi, S. & Hashimoto, K. Nitrogen-doped carbon nanomaterials as non-metal electrocatalysts for water oxidation. *Nature Commun.* **4,** 2390 (2013).
21. Tian, J., Liu, Q., Asiri, A. M., Alamry, K. A. & Sun, X. Ultrathin graphitic C_3N_4 nanosheets/graphene composites: efficient organic electrocatalyst for oxygen evolution reaction. *ChemSusChem* **7,** 2125–2130 (2014).
22. Ng, J. W. D., Tang, M. & Jaramillo, T. F. A carbon-free, precious-metal-free, high-performance O_2 electrode for regenerative fuel cells and metal–air batteries. *Energy Environ. Sci.* **7,** 2017–2024 (2014).
23. Chen, S., Duan, J., Jaroniec, M. & Qiao, S-Z. Nitrogen and oxygen dual-doped carbon hydrogel film as a substrate-free electrode for highly efficient oxygen evolution reaction. *Adv. Mater.* **26,** 2925–2930 (2014).
24. Ma, T. Y., Dai, S., Jaroniec, M. & Qiao, S. Z. Graphitic carbon ntride nanosheet–carbon nanotube three-dimensional porous composites as high-performance oxygen evolution electrocatalysts. *Angew. Chem. Int. Ed.* **53,** 7281–7285 (2014).
25. Prabu, M., Ramakrishnan, P. & Shanmugam, S. $CoMn_2O_4$ nanoparticles anchored on nitrogen-doped graphene nanosheets as bifunctional electrocatalyst for rechargeable zinc–air battery. *Electrochem. Commun.* **41,** 59–63 (2014).
26. Sun, C. *et al.* Graphene–Co_3O_4 nanocomposite as an efficient bifunctional catalyst for lithium–air batteries. *J. Mater. Chem. A* **2,** 7188–7196 (2014).
27. Tian, G-L. *et al.* Nitrogen-doped graphene/carbon nanotube hybrids: *in situ* formation on bifunctional catalysts and their superior electrocatalytic activity for oxygen evolution/reduction reaction. *Small* **10,** 2251–2259 (2014).
28. Pan, L. *et al.* Hierarchical nanostructured conducting polymer hydrogel with high electrochemical activity. *Proc. Natl Acad. Sci. USA* **109,** 9287–9292 (2012).
29. Yang, D-S., Bhattacharjya, D., Inamdar, S., Park, J. & Yu, J-S. Phosphorus-doped ordered mesoporous carbons with different lengths as efficient metal-free electrocatalysts for oxygen reduction reaction in alkaline media. *J. Am. Chem. Soc.* **134,** 16127–16130 (2012).
30. Zhang, J., Jiang, J., Li, H. & Zhao, X. S. A high-performance asymmetric supercapacitor fabricated with graphene-based electrodes. *Energy Environ. Sci.* **4,** 4009–4015 (2011).
31. Ding, W. *et al.* Space-confinement-induced synthesis of pyridinic- and pyrrolic-nitrogen-doped graphene for the catalysis of oxygen reduction. *Angew. Chem. Int. Ed.* **52,** 11755–11759 (2013).
32. Su, F. *et al.* Nitrogen-containing microporous carbon nanospheres with improved capacitive properties. *Energy Environ. Sci.* **4,** 717–724 (2011).
33. Cui, X. *et al.* Microstructure and corrosion resistance of phytic acid conversion coatings for magnesium alloy. *Appl. Surf. Sci.* **255,** 2098–2103 (2008).
34. Gorham, J., Torres, J., Wolfe, G., d'Agostino, A. & Fairbrother, D. H. Surface reactions of molecular and atomic oxygen with carbon phosphide films. *J. Phys. Chem. B* **109,** 20379–20386 (2005).
35. Puziy, A. M., Poddubnaya, O. I., Socha, R. P., Gurgul, J. & Wisniewski, M. XPS and NMR studies of phosphoric acid activated carbons. *Carbon* **46,** 2113–2123 (2008).
36. Yang, S., Feng, X., Wang, X. & Müllen, K. Graphene-based carbon nitride nanosheets as efficient metal-free electrocatalysts for oxygen reduction reactions. *Angew. Chem. Int. Ed.* **50,** 5339–5343 (2011).
37. Zhao, Y., Watanabe, K. & Hashimoto, K. Self-supporting oxygen reduction electrocatalysts made from a nitrogen-rich network polymer. *J. Am. Chem. Soc.* **134,** 19528–19531 (2012).
38. Xiang, Z. *et al.* Highly efficient electrocatalysts for oxygen reduction based on 2D covalent organic polymers complexed with non-precious metals. *Angew. Chem. Int. Ed.* **53,** 2433–2437 (2014).
39. Li, M., Zhang, L., Xu, Q., Niu, J. & Xia, Z. N-doped graphene as catalysts for oxygen reduction and oxygen evolution reactions: theoretical considerations. *J. Catal.* **314,** 66–72 (2014).
40. Sha, Y., Yu, T. H., Liu, Y., Merinov, B. V. & Goddard, W. A. Theoretical study of solvent effects on the platinum-catalyzed oxygen reduction reaction. *J. Phys. Chem. Lett.* **1,** 856–861 (2010).
41. Yu, L., Pan, X., Cao, X., Hu, P. & Bao, X. Oxygen reduction reaction mechanism on nitrogen-doped graphene: a density functional theory study. *J. Catal.* **282,** 183–190 (2011).
42. Man, I. C. *et al.* Universality in oxygen evolution electrocatalysis on oxide surfaces. *ChemCatChem* **3,** 1159–1165 (2011).
43. Du, G. *et al.* Co_3O_4 nanoparticle-modified MnO_2 nanotube bifunctional oxygen cathode catalysts for rechargeable zinc–air batteries. *Nanoscale* **5,** 4657–4661 (2013).
44. Toussaint, G., Stevens, P., Akrour, L., Rouget, R. & Fourgeot, F. Development of a rechargeable zinc–air battery. *ECS Trans.* **28,** 25–34 (2010).
45. Lee, D. U., Choi, J-Y., Feng, K., Park, H. W. & Chen, Z. Advanced extremely durable 3D bifunctional air electrodes for rechargeable zinc–air batteries. *Adv. Energy Mater.* **4,** 1301089 (2014).
46. Chen, S., Duan, J., Ran, J., Jaroniec, M. & Qiao, S. Z. N-doped graphene film-confined nickel nanoparticles as a highly efficient three-dimensional oxygen evolution electrocatalyst. *Energy Environ. Sci.* **6,** 3693–3699 (2013).
47. Nørskov, J. K. *et al.* Origin of the overpotential for oxygen reduction at a fuel-cell cathode. *J. Phys. Chem. B* **108,** 17886–17892 (2004).
48. Bao, X. *et al.* A first-principles study of the role of quaternary-N doping on the oxygen reduction reaction activity and selectivity of graphene edge sites. *Top. Catal.* **56,** 1623–1633 (2013).
49. Zhang, L. & Xia, Z. Mechanisms of oxygen reduction reaction on nitrogen-doped graphene for fuel cells. *J. Phys. Chem. C* **115,** 11170–11176 (2011).

Acknowledgements

This work is supported financially by the Air Force Office of Scientific Research (AFOSR; FA-9550-12-1-0069 and FA9550-12-1-0037) and the National Science Foundation (NSF-AIR-IIP-1343270 and NSF-CMMI-1363123). The authors thank Z. Xiang, H. Pan, Y. Xue, Y. Yu and L. Zhang for discussions and help.

Author contributions

J.Z. and L.D. conceived and designed the experiments. J.Z. performed sample characterization and electrochemical studies. Z.Z. and Z.X. performed the theoretical calculation. J.Z. and L.D. analysed experimental data and wrote the paper. All authors discussed the results and commented on the manuscript.

Additional information

Supplementary information is available in the online version of the paper. Reprints and permission information is available online at www.nature.com/reprints. Correspondence and requests for materials should be addressed to L.D.

Competing financial interests

The authors declare no competing financial interests.